SUPPORTING MATERIAL:

Membrane Cholesterol Strongly Influences Confined Diffusion of Prestin

R. I. Kamar, L. E. Organ-Darling, and R. M. Raphael*

*Correspondence: rraphael@rice.edu

MATERIALS AND METHODS

Plasmid expression and cell culture

A plasmid encoding for prestin-SNAP-tag C-terminal fusion protein was created by PCR amplifying SNAP-tag from pSS26b plasmid (Covalys, now New England BioLabs, Ipswich, MA) using forward/reverse primers 5'-tttggtacccatggacaaagattgc-3' and 5'-atatgcggccgcttatcccagacccggttta-3'. Using restriction sites KpnI and NotI, we digested out the YFP gene fragment from a prestin-YFP plasmid (gerbil-prestin gene, accession number AF230376, previously sub-cloned (1) into multiple cloning site of pEYFP-N1, Clontech, Mountain View, CA). SNAP-tag PCR fragments were finally ligated into digested prestin-YFP plasmid using the same restriction sites and then verified by sequencing.

HEK293 cells were grown in 6-well plates containing culture media consisting of phenol-red free DMEM supplemented with 10% BCS (Invitrogen, Carlsbad, CA), 1% penicillin-streptomycin, 14.3 mM HEPES, 16.1 mM $NaHCO_3$, and 4 mM L-glutamine at 37°C, 5% CO_2. Cells below passage 30 were transfected with prestin-SNAP-tag plasmid using Fugene 6 transfection reagent (Roche, Indianapolis, IN) according to manufacturer instructions.

Cells were rinsed with culture media 12-24 hours after transfection. Labeling solution containing 3µM SNAP-Cell TMR-Star fluorescent substrate (New England BioLabs) in 400µL of culture media was added to cells in the 6-well dish and incubated at 37°C for 20 min to allow substrate to covalently bind to expressed prestin-SNAP-tag fusions. Cells were then rinsed once again in substrate-free culture media before being mechanically dislodged and centrifuged in a 15 mL conical tube for three min. Natant media was aspirated from pelleted cells, and cells were resuspended and centrifuged twice more in culture media to remove excess fluorescent substrate. Cells were then incubated for 30 min in substrate-free media at 37°C and replaced with fresh media one more time to remove substrate that leaked out of cells. Cells are then cultured on RCA cleaned (2) #1.5 coverslips for 24 hours before imaging. For imaging, coverslips containing low density of adherent cells were first rinsed with HEPES buffered saline (HBS, contents in mM: dextrose 5.6, HEPES 21, KCl 5, NaCl 13.7, Na_2HPO_4 0.76, pH adjusted to 7.4, osmolarity 300 mOsm). Coverslips with adherent cells were finally mounted on a microscope viewing chamber with vacuum grease and bathed with HBS.

Single molecule microscopy and trajectory calculation

Live HEK293 cells expressing prestin-SNAP-TMR (prestin-SNAP-tag labeled with SNAP-Cell TMR-Star) were imaged at room temperature on an inverted Zeiss Axiovert microscope using objective-type total internal reflection (TIR) (3). Tetramethylrhodamine (TMR) fluorophores are excited using 10-11 mW of 514 nm light from an Ar^+ laser. Light is made circularly polarized with a λ/4 waveplate (Thorlabs, Newton, NJ) placed in the beam path at 45° to the polarization of the laser. Prior to placing the laser in TIR configuration, we estimate the intensity to be ~100 W/cm^2. Fluorescence is collected with a 100X, 1.45NA microscope objective and filtered in a band from 550-600 nm. Detection of TMR fluorescence, which appears as diffraction limited fluorescent spots, is captured on a force-air-cooled, back illuminated QuantEM EMCCD camera (Photometrics, Tucson, AZ) run with open source Micro-Manager plugin software to ImageJ. Prior to image acquisition sequence, a large fraction of prestin-SNAP-TMR molecules are photobleached using the laser until the density of fluorescent molecules is low enough to preserve identification of fluorescent spots between frames. Image stacks 200 frames long are captured with a frame time Δt = 250.8 ms (~4 frames/s) and exposure time t_{ill}=250 ms. Frame sizes are 256×256 pixels and, using a reticule to measure the magnification, the height and width of each pixel is measured to correspond to 156.9±0.7×10^{-3} μm/pixel in the object plane.

Individual fluorescent spots in each frame are detected and analyzed using homemade analysis software in MATLAB (The MathWorks, Natick, MA). The position (x_o,y_o) and positioning errors of each spot in every frame is determined by fitting the signal profile $\Psi(x,y)$ to

$$\Psi(x,y) = \frac{4I_o \ln 2}{\pi s^2} \exp\left\{\frac{-4\ln 2}{s^2}\left((x-x_o)^2 + (y-y_o)^2\right)\right\} + b \qquad \text{(S1)}$$

where I_o is the spot intensity, s is the full-width at half-maximum, and b is the background level. Trajectories are generated (Fig. 1 in main text) using a combination of software, which allows for correlation of spots between images, and correlation by hand. For each trajectory, the squared deviation $d^2(t_{lag})$ is calculated at every time $t_{lag}=(n-1)\Delta t$ (where n is the frame number, n=1 referring to the first observation of the particle) according to

$$d^2(t_{lag}) = \left(x_o(t_{lag}) - x_o(0)\right)^2 + \left(y_o(t_{lag}) - y_o(0)\right)^2 \qquad \text{(S2)}$$

where $x_o(t_{lag})$ and $y_o(t_{lag})$ are the x and y coordinates of the particle at time t_{lag}, and $x_o(0)$ and $y_o(0)$ are the coordinates of the first observation of the particle. The mean-squared deviation $MSD(t_{lag})$ at time t_{lag} is calculated as an average of all the tracks according to

$$MSD(t_{lag}) = \left(\frac{1}{N_T(t_{lag})}\right) \sum_{i=1}^{N_T(t_{lag})} d_i^{\,2}(t_{lag}) \qquad \text{(S3)}$$

where the subscript i has been added to run over all $N_T(t_{lag})$ trajectories. The mean-squared deviation data is corrected for finite position accuracy σ_{xy} by subtracting from the MSD an offset Δ that the non-zero position uncertainty produces (4). Both σ_{xy} and Δ are determined by measuring the position of immobile prestin-SNAP-TMR molecules in

fixed cells and using Eqs. S2 and S3 to calculate Δ, and ascribing the standard deviation in position to σ_{xy} (see Supplemental Results and Fig. S1).

SUPPLEMENTAL RESULTS

Characterization of position accuracy effects

Since a finite positional accuracy will introduce systematic errors into the measurement of *MSD* (5), it is important to characterize and understand the effects those errors produce. We therefore estimated the localization error σ_{xy} by measuring the standard deviation in x-position σ_x of immobilized prestin-SNAP-TMR molecules over many frames. For each observed particle *i*, we also measure the apparent squared displacement $d_i^2(t_{lag})$ which is a measure of the offset Δ_i the error σ_x produces. Shown in Fig. S1A is Δ_i versus σ_x confirming the relationship $\Delta=4\sigma_{xy}^2$. We measure the overall offset Δ that should be subtracted from the diffusion data by calculating the apparent *MSD* of the immobile particles in fixed cells using Eq. S3. The result is shown in Fig. S1B giving $\Delta=1.91\pm0.08\times10^{-3}\mu m^2$. Because the position uncertainty is dependent on the brightness (6) of the particles, which varies between fluorescent spots, we measure a spread of uncertainties (Fig. S1C). This effect is automatically taken into account in the measurement of Δ in Fig. S1B since it is measured from an ensemble of particles that have a brightness distribution representative of that in live cell experiments.

Effects of varying position accuracy on localization offset

When trying to discriminate between hop-diffusion and free diffusion, Wieser et. al. (7) have shown that precise determination of the confinement offset *CO* is required to simultaneously determine D_{micro}, $\hat{\tau}$, and L in cases where the time resolution Δt is greater than τ_{micro}. This requires precise determination of the localization error offset Δ (5). We have shown that spread in σ_{xy} can cause a significant error in Δ if one simply estimates the average standard deviation in position localization $\bar{\sigma}_{xy}$ and assumes $\Delta = 4\bar{\sigma}_{xy}^2$ (Fig. S2). In our study we estimated the average localization error to be 19.9 nm with a spread of 8.4 nm (Fig. S1). Assuming $\Delta=4\times(19.9\text{ nm})^2$ would have implied $\Delta=1.58\times10^{-3}\mu m^2$. However, we demonstrated using a Monte Carlo simulation (Figs. S2 and S3) that the actual offset this would produce is $1.88\times10^{-3}\mu m^2$ demonstrating a systematic underestimate of $0.3\times10^{-3}\mu m^2$, nearly four times the statistical error in our measurement of Δ! Thus it is important to measure Δ directly by measuring *MSD* for immobilized particles, as illustrated in Fig. S1B.

Fitting of CDFs at short time lag

We measured the CDF of squared step-size $P(\Delta r^2, t_{lag}=250.8ms)$ at a time lag $t_{lag} = 250.8ms$ for both treatment groups (Fig. S4). Using Eq. 3 (main text) to fit the CDF of squared displacements, with the inclusion of $F(\Delta r^2)$ (Fig. S3) to account for the apparent immobility of displacements within small corrals, improved the fits considerably compared to a simple pure exponential $1-\exp(-\Delta r^2 / r_o^2)$, although some deviations are still apparent (Figs. S4A and B). For the untreated group, the fitting gave $D = 0.0401\mu m^2/s$ and $\varepsilon = 0.6222$, and for MβCD we obtained $D = 0.0477\mu m^2/s$ and $\varepsilon = 0.684$. According to our argument that displacements in the smallest confinements

appear immobile, depletion of membrane cholesterol decreases the apparent fraction $(1-\varepsilon)$ of molecules confined to domains with size << 95 *nm* from 37.8 to 31.6% (an absolute difference of 6.2%) at $t_{lag} = 250.8 ms$. This is consistent with a shift to larger domain sizes. The diffusion constant for the MβCD group is in reasonable agreement with that obtained from *MSD* analysis. However, for the untreated group the diffusion constant using CDF analysis is 17% lower than that obtained using *MSD* analysis.

Effects of detector averaging and non-uniform corral size

For long exposure times (as we have here) the CDFs in Fig. S4 should not fit to a pure exponential due to detector averaging effects even for a constant domain size *L*. As explained in Wieser et al. (7), the probability for apparent small displacements is enhanced for exposure times that are not short compared to t_{lag} (as observed in Figs. S4A and B, insets) since positional averaging biases the trajectory to the center of the domain causing a steeper increase of the CDF as shown in Fig. S4C. If, as we had originally assumed, there was a narrow domain size distribution peaked around the averages determined from *MSD* analysis (~1-2 μm), the effect would be minimal. This is because $t_{ill} = 250 ms$ is much less than the microscopic residence time (8) $\tau_{micro} = L^2 / 4D_{micro}$ which is 8 *s* for the untreated group and 23 *s* for MβCD treated group. However, since we have a range of domain sizes that extends toward small domains, as evidenced by both the large values of $(1-\varepsilon)$ and the observation in Fig. 1 (main text) of confinement regions of varying size, the effects of time averaging on the distribution of squared-displacements should enhance the probability for small displacements occurring within domains even somewhat larger than 95 *nm* (see Fig. S5A). To compare the relative effect on each treatment group, we subtracted the probability density distributions (Fig. S5B). We observe a peak in the difference distribution $\delta p(\Delta r^2) = p_{untreated}(\Delta r^2) - p_{M\beta CD}(\Delta r^2)$ out to Δr^2 of $0.01-0.02\,\mu m^2$ beyond which the difference is nearly flat. The sum of the probabilities out to Δr^2 of $0.02\,\mu m^2$ is 7±1% in agreement with the difference of $(1-\varepsilon)$ between groups.

Recently, the effects of detector averaging on confined diffusion have been well characterized (5,8,9) showing that the probability for small displacements appears increased within small confinements. That the diffusion coefficient obtained from the fit to $P(\Delta r^2, t_{lag} = 250.8 ms)$ of the MβCD treated group was in reasonable agreement with D_{micro} obtained from *MSD* analysis, while that of the untreated group noticeably differed, suggests that cholesterol depletion reduces the density of small domains compared to the untreated group leaving the latter more prone to the effects of detector averaging. This effect is illustrated in Fig. S5A which shows that detector averaging effects become rapidly more pronounced for smaller domains. The difference between the probability density distributions (Fig. S5B) showed a sharp relative increase in the effect for the untreated group for Δr^2 in a range from zero to $0.15\,\mu m^2$ further indicating an increasing shift in average confinement size. This is consistent with the larger average domain size obtained from *MSD* analysis for the MβCD treated group. The closer resemblance to Brownian diffusion for the MβCD CDF is also explained by the 75% reduced

confinement strength $\hat{\tau}$ since as $\hat{\tau} \to 1$ free diffusion is recovered (5). This is illustrated in Fig. S5C which shows that $MSD_{hop}(t_{lag} = 250.8\,ms)$ predicted for the MβCD group is closer to $4D_{micro}t_{lag}$ than the untreated group, especially for small domain sizes, since it has an α value closer to zero.

SUPPLEMENTAL FIGURES

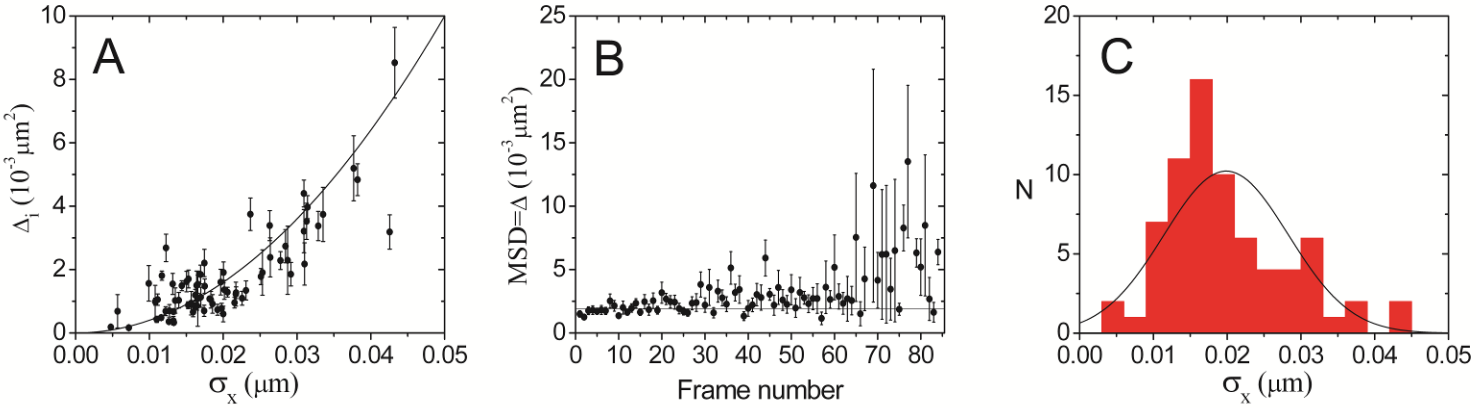

Figure S1. Analysis of positioning error and offset. (A) Plot of apparent average offset Δ_i against standard deviation in repeated measurement of x-position σ_x of 72 individual immobile fluorescent spots. Solid curve is the relation $\Delta = 4\sigma_{xy}^2$. Error bars are error of the mean. (B) Plot of *MSD*, calculated using Eq. S3, of all 72 immobilized trajectories against frame number. Error bars are error of the mean. Data is fit to $MSD = \Delta$ and is weighted by error bars. Increased variance at high frame numbers is due to decreased probability of a particle remaining fluorescent at long times. Fit gives $\Delta = 1.91 \pm 0.08 \times 10^{-3} \mu m^2$, $\chi_\nu^2 = 1.8$. Measured offset implies localization error $\sigma_{xy} = 22\,nm$. (C) Histogram of measured standard deviations σ_x characterized by sample mean $\bar{\sigma}_x = 19.9\,nm$ and spread $\sigma_{\sigma_x} = 8.4\,nm$. Although obviously skewed, we approximated the distribution by a Gaussian (solid curve) with the measured sample mean $\bar{\sigma}_x$ and standard deviation σ_{σ_x}.

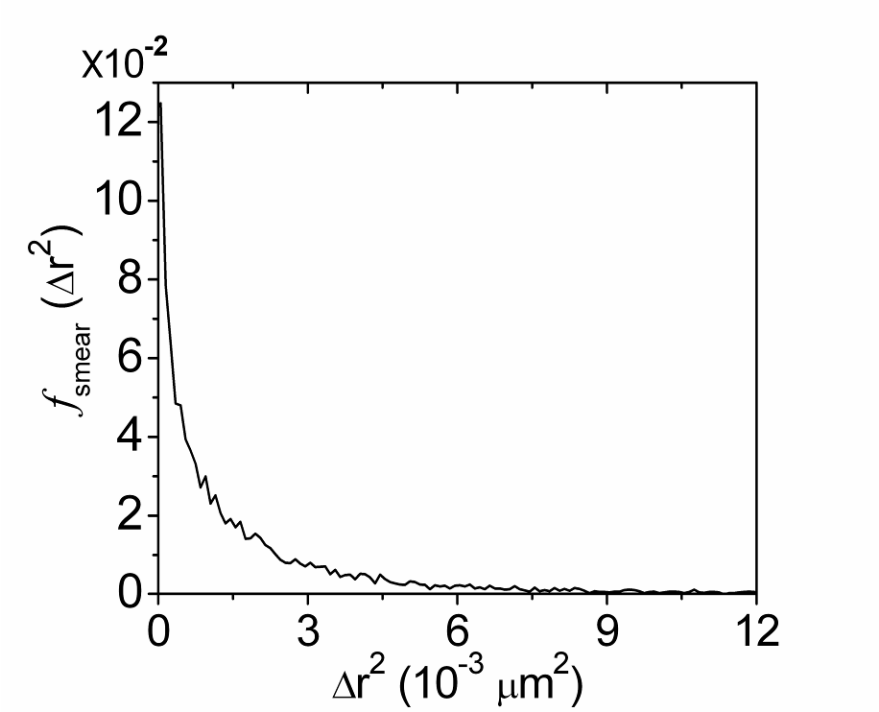

Figure S2. Simulation of probability density of immobile particle apparent displacements. Shown is the probability density generated by assuming a Gaussian distribution of immobile particle position uncertainties reported in Fig. S1. Simulated error is squared distance $\left|(\vec{r}_2 - \vec{r}_1)\right|^2$ between two position measurements, $\vec{r}_1 = (\delta x_1, \delta y_1)$ and $\vec{r}_2 = (\delta x_2, \delta y_2)$, where the errors δx_1, δy_1, δx_2, and δy_2 are randomly generated from a Gaussian distribution with zero mean and standard deviation randomly selected from another Gaussian distribution with mean of $19.9\,nm$ and standard deviation $8.4\,nm$ (see Eq. 4 in main text for the form of $f_{smear}(\Delta r^2)$). Displayed distribution is a normalized histogram of 30,000 simulations. The mean of the simulated distribution is $\Delta_{simulation} = 1.88\times10^{-3}\,\mu m^2$ in excellent agreement with measured $\Delta = 1.91 \pm .08\times10^{-3}\,\mu m^2$. Assuming $\Delta = 4\bar{\sigma}_x^{\,2} = 4(19.9\,nm)^2 = 1.58\times10^{-3}\,\mu m^2$ under-estimates $\Delta_{simulation}$ by $0.3\times10^{-3}\,\mu m^2$.

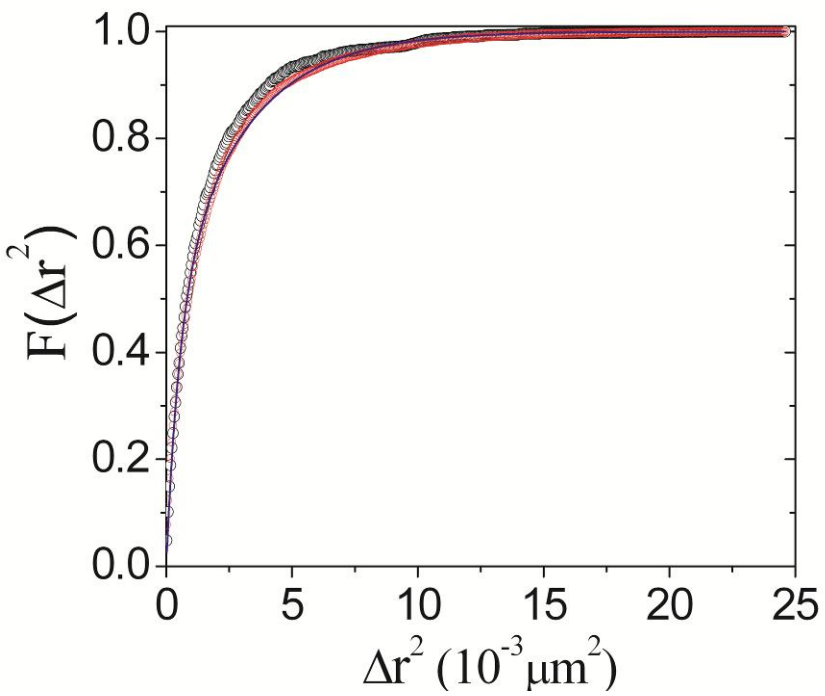

Figure S3. CDF of immobile particle apparent displacements. Black circles represent the measured CDF of immobile particles. Red circles represent the CDF $F(\Delta r^2)$ generated by assuming a distribution of position errors according to those measured in Fig. S1. See Results in main text for a detailed explanation of this calculation. For the purposes of including $F(\Delta r^2)$ in $P(\Delta r^2)$ (Eq. 3 in main text), $F(\Delta r^2)$ is approximated by an empirical fit to a bi-exponential ($\mathrm{F}\left(\Delta r^2\right) = 1 - 0.546542\,\mathrm{e}^{-\Delta r^2/0.00287\,\mu\mathrm{m}^2} - 0.453458\,\mathrm{e}^{-\Delta r^2/0.00052\,\mu\mathrm{m}^2}$, blue curve).

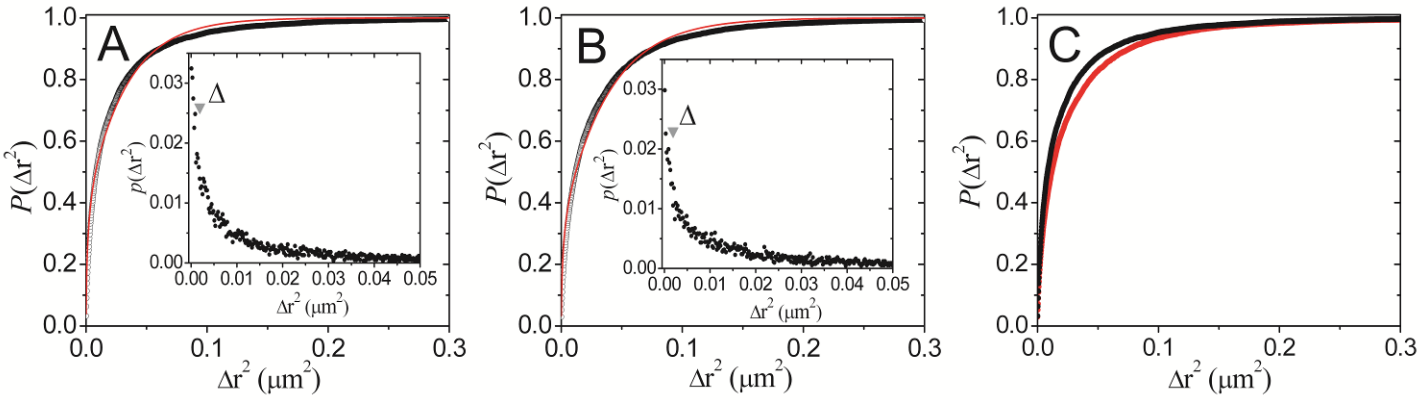

Figure S4. Statistical distributions of squared step-size. CDF at $t_{lag} = 250.8 ms$ of (A) untreated (black circles appear like a thick line due to high density of points) and (B) MβCD treated groups. Fits of CDF using Eq. 3, in main text, are shown as red lines in (A) and (B). Insets show the original probability density (black circles) on a zoomed in scale; the position of the localization offset Δ (see Fig. S1B) is shown with gray arrows. The probability density $p(\Delta r^2)$ of short displacements for both groups rises quicker than an exponential rise explaining why the CDFs do not fit to a pure exponential expected for simple free diffusion. (C) CDF of untreated (black circles) and MβCD (red circles) groups are re-plotted on the same graph for comparison.

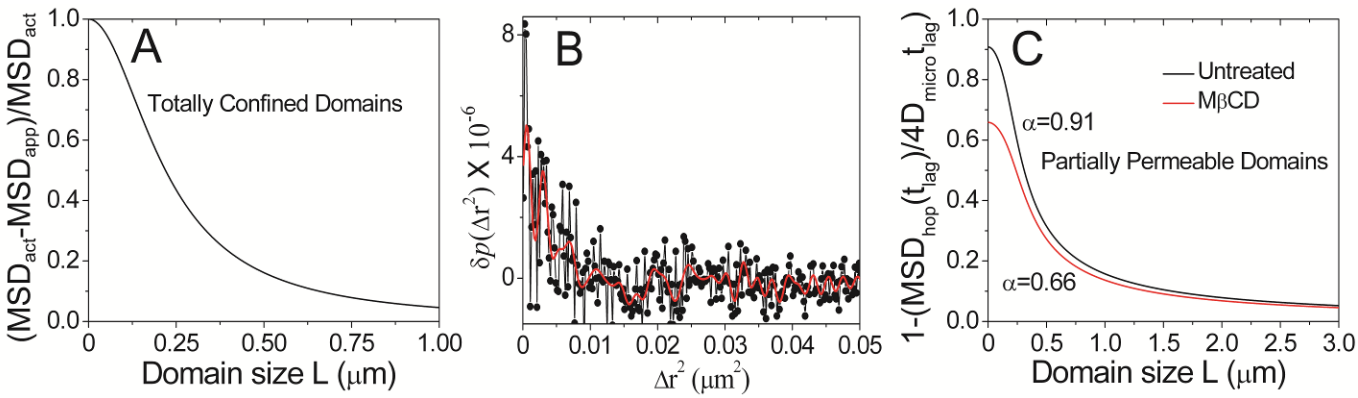

Figure S5. Effect of detector averaging, L, and $\hat{\tau}$ on step-size distribution. (A) Plot of the error in $MSD(t_{lag} = 250.8\,ms)$ detector averaging over 250 ms would produce as a function of L for impermeable domains ($D_{micro} = 0.048\,\mu m^2/s$). (B) Difference of untreated and MβCD treated probability density distributions ($\delta p(\Delta r^2) = p_{untreated}(\Delta r^2) - p_{M\beta CD}(\Delta r^2)$, solid circles). Also shown is $\delta p(\Delta r^2)$ low-pass filtered at $500\,\mu m^{-2}$ (red curve). Sum of probabilities out to $\Delta r^2 = 0.02\mu m^2$ is 7±1%. (C) Plot of $1 - \dfrac{MSD_{hop}(t_{lag} = 250.8\,ms)}{4D_{micro} \times 250.8\,ms}$ in partially permeable domains as a function of L, using α and D_{micro} obtained from fitting $MSD(t_{lag})$, for untreated and MβCD groups. Here $MSD_{hop}(t_{lag})$ is Eq. 1 (main text) with $t_{ill} = 0$.

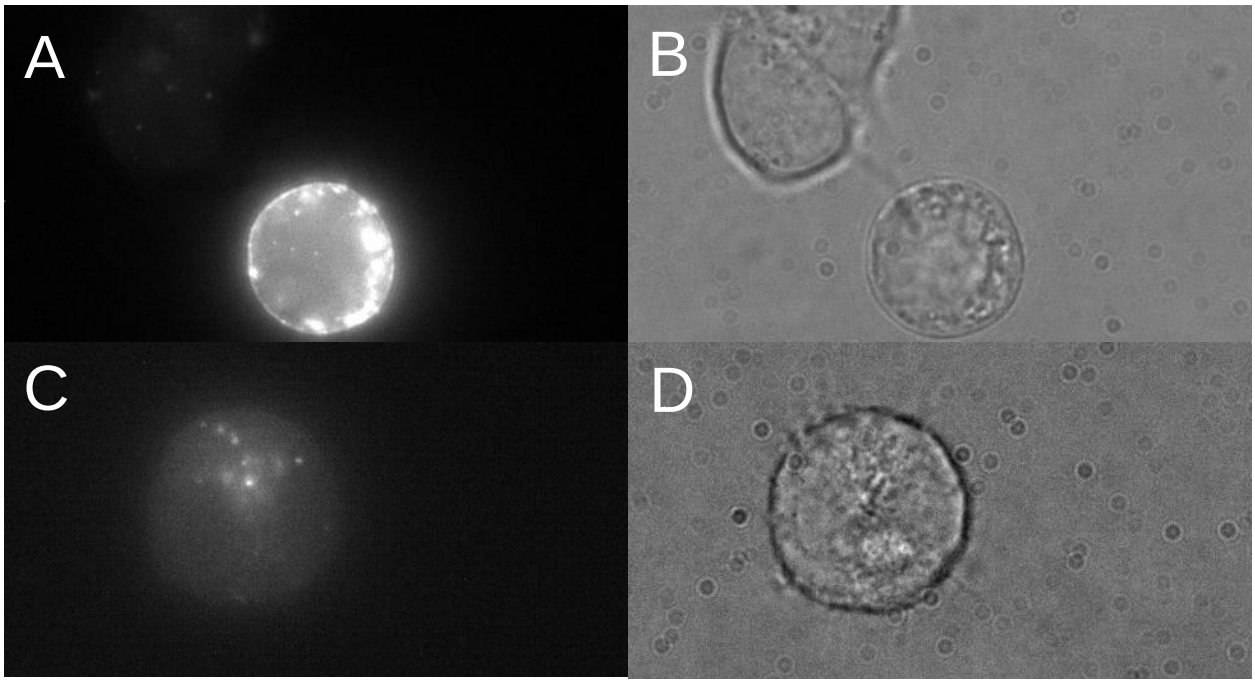

Figure S6. Comparison of transfected and untransfected cells. Top panels, (A) and (B), contain corresponding images of cells obtained from a group of cells transfected with prestin-SNAP-tag and labeled with TMR-Star. Bottom panels, (C) and (D), contain corresponding images of a cell obtained from a group that was not exposed to any plasmid but was labeled with TMR-Star under the same conditions as (A) and (B). Panels (A) and (C) are fluorescence images obtained using wide field epi-illumination, while panels (B) and (D) are white light transmission images in the same respective fields of view. In panels (A) and (B) the cell in the bottom middle of the image is clearly transfected (note the clear membrane targeting of fluorescence), while the cells in the top left corner either did not take up any plasmid or have low expression. Compare panels (A) and (B) with Movie S3 which is obtained using TIRF in the same field of view. Compare panels (C) and (D) with Movie S4 obtained using TIRF in the same field of view. All panels are 65.4 μm × 122 μm. Note that non-specific labeling of TMR-Star is mainly restricted to intracellular compartments. Conditions for fluorescence microscopy in this figure are different than those in the main text in the following ways. Excitation is ~4-5 mW of 532 nm light from a Millenia IIs diode-pumped cw laser (Spectra Physics, Mountain View, CA). TMR fluorescence is collected in a band from 570 – 640 nm and imaged onto the Zeiss MRm CCD camera.

SUPPORTING REFERENCES

1. Greeson, J. N., L. E. Organ, F. A. Pereira, and R. M. Raphael, 2006. Assessment of prestin self-association using fluorescence resonance energy transfer. *Brain Res* 1091:140-150.

2. van Dam, R. M., 2005. Solvent-Resistant Elastomeric Microfluidic Devices and Applications. Ph.D. thesis, California Institute of Technology.

3. Axelrod, D., T. P. Burghardt, and N. L. Thompson, 1984. Total internal reflection fluorescence. *Annu Rev Biophys Bioeng* 13:247-268.

4. Martin, D. S., M. B. Forstner, and J. A. Käs, 2002. Apparent subdiffusion inherent to single particle tracking. *Biophys J* 83:2109-2117.

5. Wieser, S., M. Moertelmaier, E. Fuertbauer, H. Stockinger, and G. J. Schütz, 2007. (Un)confined diffusion of CD59 in the plasma membrane determined by high-resolution single molecule microscopy. *Biophys J* 92:3719-3728.

6. Thompson, R. E., D. R. Larson, and W. W. Webb, 2002. Precise nanometer localization analysis for individual fluorescent probes. *Biophys J* 82:2775-2783.

7. Wieser, S., M. Axmann, and G. J. Schütz, 2008. Versatile analysis of single-molecule tracking data by comprehensive testing against Monte Carlo simulations. *Biophys J* 95:5988-6001.

8. Destainville, N., and L. Salomé, 2006. Quantification and correction of systematic errors due to detector time-averaging in single-molecule tracking experiments. *Biophys J* 90:L17-L19.

9. Ritchie, K., X.-Y. Shan, J. Kondo, K. Iwasawa, T. Fujiwara, and A. Kusumi, 2005. Detection of non-Brownian diffusion in the cell membrane in single molecule tracking. *Biophys J* 88:2266-2277.

Figure legends for Movies S1-5

Movie S1. Image stack of transfected cell not treated with MβCD. The region of interest (ROI) is 11 μm × 10 μm. Fluorescence images obtained using TIRF. Trajectories from this cell were included in the reported control data in the main text.

Movie S2. Image stack of transfected cell treated with MβCD. ROI is 11.3 μm × 7.8 μm. Fluorescence images obtained using TIRF. Trajectories from this cell were included in the reported MβCD data in main text.

Movie S3. TIRF image stack of transfected cells treated with TMR-Star. Same cells and field of view as Figs. S6A and B. Note that the cell in the bottom middle portion of the image displays numerous diffusing diffraction-limited signals while the cells in the top left do not.

Movie S4. TIRF image stack of untransfected cell treated with TMR-Star. Same cell and field of view as Figs. S6C and D. Note that the whole cell displays a total of only ~3-4 diffusing diffraction-limited signals confirming that nonspecific labeling of TMR-Star is low and restricted to mainly intracellular compartments. Compare this to Movie S5.

Movie S5. TIRF image stack of transfected cell treated with TMR-Star. The entire coverslip-adhered portion of cell membrane is visible in the field of view (63.4 μm × 63.9 μm). Note the high density of diffusing diffraction-limited signals compared with Movie S4. Transfected cells require several minutes of pre-photobleaching with laser before individual diffraction-limited signals are observable due to the high level of fluorescence.